Implementation of the Constant Current and Constant Voltage Charge of Inductive Power Transfer Systems With the Double-Sided *LCC* Compensation Topology for Electric Vehicle Battery Charge Applications

Van-Binh Vu, *Student Member, IEEE*, Duc-Hung Tran, and Woojin Choi, *Member, IEEE*

***Abstract*—When compared to plugged-in chargers, inductive power transfer (IPT) methods for electric vehicle (EV) battery chargers have several benefits, such as greater convenience and higher safety. In an EV, the battery is an indispensable component, and lithium-ion batteries are identified as the most competitive candidate to be used in EVs due to their high power density, long cycle life, and better safety. In order to charge lithium-ion batteries, constant current/constant voltage (CC/CV) is often adopted for high-efficiency charging and sufficient protection. However, it is not easy to design an IPT battery charger that can charge the batteries with a CC/CV charge due to the wide range of load variations, because it requires a wide range of variation in its operating frequency, duty, or phase-shift. Furthermore, zero phase angle (ZPA) condition for the primary inverter cannot be achieved over the entire charge process without the help of additional switches and related driver circuits to transform the topology. This paper proposes a design method that makes it possible to implement the CC/CV mode charge with minimum frequency variation during the entire charge process by using the load-independent characteristics of an IPT system under the ZPA condition without any additional switches. A theoretical analysis is presented to provide the appropriate procedure to design the double-sided *LCC* compensation tank which can achieve both CC and CV mode charge under ZPA condition at two different resonant frequencies. As a consequence, the proposed method is advantageous in that the efficiency of compensation tank is very high due to achieving the perfect resonant operation during the entire charge process. A 6.6-kW prototype charger has been implemented to demonstrate the feasibility and validity of the proposed method. A maximum efficiency of 96.1% has been achieved with a 200-mm airgap at 6.6 kW during the CC mode charge.**

***Index Terms*—Constant current/constant voltage (CC/CV) charge, electric vehicle (EV) battery charge, inductive power transfer (IPT), *LCC* compensation circuit.**

Manuscript received April 26, 2017; revised July 18, 2017 and September 8, 2017; accepted October 19, 2017. Date of publication October 25, 2017; date of current version June 22, 2018. Recommended for publication by Associate Editor S. Williamson. *(Corresponding Author: Woojin Choi.)*

V. B. Vu was with Newcastle University, Newcastle Upon Tyne NE1 7RU, U.K. He is now with the Electrical Engineering Department, Soongsil University, Seoul 06978, South Korea (e-mail: V.B.Vu2@ncl.ac.uk).

D. H. Tran is with the Electrical Engineering Department, Soongsil University, Seoul 06978, South Korea (e-mail: duchungdktd@gmail.com).

W. Choi is with the Electrical Engineering Department, Soongsil University, Seoul 156-743, South Korea (e-mail: cwj777@ssu.ac.kr).

Color versions of one or more of the figures in this paper are available online at http://ieeexplore.ieee.org.

Digital Object Identifier 10.1109/TPEL.2017.2766605

I. Introduction

ELECTRIC VEHICLES (EVs) have recently received a great deal of attention due to their clean, efficient, and environmentally friendly nature [1]. Nowadays, most commercial EVs are plugged into the grid to charge their batteries. Due to advantages such as increased user convenience and better safety in comparison to plug-in chargers, inductive power transfer (IPT) in EVs has been researched and developed by many laboratories and companies all over the world [1], [2].

A set of loosely coupled coils instead of a conventional transformer is the major difference between an IPT charger and a conductive charger. One problem with IPT systems is their lower coupling coefficient between the transmitter and receiver coils, which results in a higher reactive power and lower power transfer efficiency. Hence, the compensation tank is an important part that contributes to a reduction in the reactive power, and an improvement in power transfer capability and overall efficiency. Depending on how the compensation capacitors are added to the primary and secondary coils, there are four basic compensation topologies, namely series-series (SS), series-parallel (SP), parallel-series (PS), and parallel-parallel (PP) [1], [3]. In addition, some other topologies are also used to improve the power transfer efficiency and to simplify the control of IPT systems [4]–[8]. An inductor–capacitor–inductor (*LCL*) topology is introduced for the vehicle-to-grid (V2G) application in [4]. In [5], the primary compensation tank is developed by adding a *LC* tank between the primary side inverter and the transmitting coil. The additional *LC* tank helps reduce the conduction losses of the primary switches by reducing the primary current. Besides, the constant current (CC) control at the output can be easily achieved by using load-independent characteristics of the converter. The unity-power-factor pickup topology is formed by adding one more *LC* circuit to the parallel compensation topology in secondary side to minimize the circulating current in the receiver coil and to achieve a unity power factor [6]. However, all of topologies in [4], [5], and [6] have to require additional inductors at each side or both sides, where the inductance values are normally similar to those of coils. In order to reduce the size and cost of the additional inductors, a *LCC* compensation topology is introduced by employing a capacitor into *LCL* primary compensation tank, which is connected in series with the primary coil

[7]. In [8], a double-sided *LCC* topology is developed in both of primary and secondary sides. This topology has all of the advantages of topologies presented in [4]–[6]. In this topology, the zero voltage switching (ZVS) condition for the switches can be achieved, and the resonant frequency is independent of the coupling coefficient and load [8]. It can be regarded as a superior advantage of the IPT system. In order to improve the compactness of double-sided *LCC* topology, the magnetic integration of additional inductors and the IPT coils is proposed and investigated in [9]–[11].

The other problem with IPT charger systems is implementing a charge process for EV batteries, which comprises CC charge and constant voltage (CV) charge. Initially, the charger charges a battery with the CC mode and the battery voltage gradually increases. When the battery voltage reaches the maximum charge voltage, the charger changes its mode from the CC mode charge to the CV mode charge. The charge process is completed when the battery current reaches a certain value (for example, 0.05 C) [12]. In order to extend the lifetime of a battery, it is necessary for a charger to provide accurate charge current and voltage through stable operations. Since batteries are considered to be varying loads during charging, the charge converter needs to regulate its output precisely to implement the CC/CV mode charge. Typically, pulse width modulation (PWM) is used for converters operating with a fixed frequency, and pulse frequency modulation (PFM) is used for those operating with a fixed duty [13], [15], and [25]. Sometimes hybrid techniques combining two different techniques of PWM and PFM are also used. When single resonant converter is used to implement the CC and CV mode charge, the PFM method is often adopted to cope with wide range of load variation. Then, a wide range of variation in the operation frequency is inevitable for the operation with a varying load [13]. This results in a high circulating current in the converter and a loss of the zero voltage switching (ZVS) or zero current switching (ZCS) characteristics. This also leads to a significant increase in the power loss and a reduction in the power transfer capability. Furthermore, it may result in a bifurcation phenomenon, where the controllability and stability of the system are lost [15]. In order to avoid these disadvantages some approaches employ a back-end dc/dc converter to control the output current or voltage, whereas the front-end converter operates at the resonant frequency to achieve the zero phase angle (ZPA) condition [14], [16], [17]. However, this increases the component counts, losses, and complexity.

In order to simplify the control of an IPT charger system and avoid the above drawbacks of conventional control methods under wide variations of the load in implementing the CC/CV charge, some researchers have started to utilize the load-independent characteristics of four basic compensation topologies at their resonant frequencies [18]–[21]. It is well known that among those topologies, the PS topology can achieve the CV charge and the PP topology can achieve the CC charge. Although the SS and SP topologies can achieve both CC and CV charge, the SS loses the ZPA condition in the CV charge, and SP loses the ZPA condition in the CC mode. To achieve the ZPA condition during the entire charge process, hybrid topologies with SS and PS or SP and PP has been proposed in [21]. However, it is necessary to use additional switches and associated driver circuits to transform the topology.

In this paper, a novel approach to implement the CC/CV charge with a double-sided *LCC* topology is introduced to overcome the aforementioned drawbacks of the conventional IPT charger. Differentiating from existing works [8]–[11], in which the authors have only focused on designing of double-sided *LCC* topology at one resonant frequency for achieving only load-independent current, a design guideline of a double-sided *LCC* compensation tank is given in this paper to achieve both load-independent current and voltage characteristics with the ZPA condition at two different resonant frequencies. Next, the load-independent current frequency is utilized for CC mode charge and the load-independent voltage frequency is utilized for CV mode charge. In each mode charge, the IPT charger can operate at a nearly fixed resonant frequency, and high efficiency can be achieved due to perfect resonant operation over the entire charge operation. The proposed IPT charger has following advantages over the conventional IPT charger.

1) Elimination of a back-end dc/dc converter, which needs to be inserted in between the resonant converter and the battery to control the current and voltage for CC and CV mode operation, respectively. Since, in many of the previous researches, the resonant converter just operates at the resonant frequency to maximize the efficiency, a back-end dc/dc converter is essential to implement the CC and CV operation. Therefore, proposed IPT charger has advantages in terms of cost, complexity, and overall efficiency.
2) No additional circuit to change the resonant tank. Unlike the hybrid topologies in [20]–[21], the proposed IPT charger does not require any additional switches and related driver circuits to change the resonant tank in implementing CC and CV mode charge operation.
3) Perfect ZPA condition and soft switching operation over the entire charge operation including both CC and CV mode charge.
4) Almost single resonant frequency operation can be achieved for each CC and CV mode charge, respectively, which helps to enhance the reliability of IPT charger by avoiding the bifurcation issue.

This paper consists of five sections. A theoretical analysis of the output characteristics and input impedances of the double-sided *LCC* topology and implementation of the CC/CV charge are presented in Section II. The design consideration for the implementation of the proposed IPT charger and closed-loop controller for each mode of charge are mentioned in Section III. In Section IV, a 6.6-kW prototype is implemented to demonstrate the validity of the proposed method, and experimental results are presented to evaluate the performance of the proposed IPT battery charger. Finally, some conclusions are given in Section V.

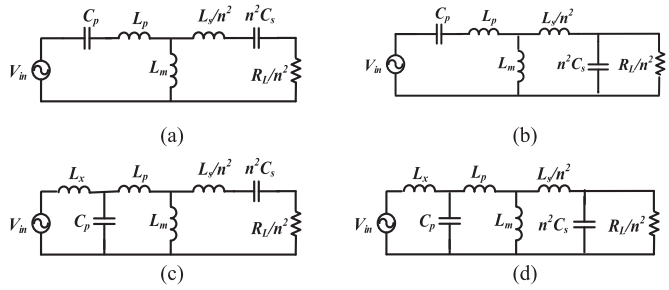

Fig. 1. AC equivalent circuits of four basic IPT topologies (a) SS. (b) SP. (c) PS. (d) PP.

II. Analysis of the Double-Sided *LCC* Converter and Implementation of the CC/CV Charge

A. Characteristics of Four Basic IPT Topologies

In this section, the output characteristics of the four basic IPT topologies SS, SP, PS, and PP are summarized to evaluate their suitability for the battery charge applications. Fig. 1(a)–(d) show the ac equivalent circuits of these topologies, where L_p and L_s are the leakage inductances of the primary and secondary coil, whereas L_m is the magnetizing inductance of the coils, C_P and C_s are the primary and secondary compensation capacitors. The turn ratio between the two coils is $1:n$.

In order to achieve the ZPA condition, the resonant frequency of the SS topology is typically chosen by

$$f_{\text{CC\_SS}} = \frac{1}{2\pi\sqrt{L_1 C_p}} = \frac{1}{2\pi\sqrt{L_2 C_s}} \tag{1}$$

where $L_1 = L_m + L_p$ and $L_2 = L_m + L_s$ are the primary and secondary self-inductance, respectively.

If L_1 and L_2 are completely compensated by the primary compensation capacitor C_p and the secondary compensation capacitor C_s, respectively, then the output current becomes load-independent and the phase of the input impedance becomes equal to zero when operating at $f_{\text{CC\_SS}}$. This means that the CC operation is possible and the ZPA condition can be achieved at $f_{\text{CC\_SS}}$. On the other hand, the SS topology has two other resonant frequencies, where the output voltage is constant regardless of the load (CV operation). Typically, a higher frequency is selected as the operating frequency in CV operation so that the resonant tank can operate in the inductive region, and the primary switches can operate under the ZVS condition

$$f_{\text{CV\_SS}} = \frac{1}{2\pi\sqrt{L_p C_p}} = \frac{1}{2\pi\sqrt{L_s C_s}}. \tag{2}$$

However, it is not desirable to operate a converter at $f_{\text{CV\_SS}}$ due to the following drawbacks. First, the high turn-off current due to the large phase of the input impedance, especially in the light load conditions, increases the switching loss and impairs the efficiency. Second, the large reactive power significantly increases the conduction loss and reduces the power transfer capability.

Similar to that in the SS topology, the CC/CV mode operation can be implemented with SP topology. While it can achieve ZPA condition when working as a load-independent voltage source, the input impedance becomes inductive when working as a load-independent current source. As a consequence, SP topology cannot achieve ZPA condition in CC mode operation. Unlike the SS and SP topologies, the PS and PP topologies can only implement the CV mode or the CC mode, respectively [1], [21].

TABLE I
Comparison of Four Basic IPT Topologies

Topology	Possible mode charge to implement	ZPA	Angular Resonant Frequency
SS	**CC**	**Yes**	$\omega = \frac{1}{\sqrt{L_1 C_p}} = \frac{1}{\sqrt{L_2 C_s}}$
	CV	**No**	$\omega = \frac{1}{\sqrt{L_p C_p}} = \frac{1}{\sqrt{L_s C_s}}$
SP	**CC**	**No**	$\omega = \frac{1}{\sqrt{L_p C_p}} = \frac{1}{\sqrt{L_s C_s}}$
	CV	**Yes**	$\omega = \frac{1}{\sqrt{1-k^2}}\frac{1}{\sqrt{L_p C_p}} = \frac{1}{\sqrt{L_2 C_s}}$
PS	**CV**	**Yes**	$\omega = \frac{1}{\sqrt{L_1 C_p}} = \frac{1}{\sqrt{L_2 C_s}}$ and $L_x = L_1$
PP	**CC**	**Yes**	$\omega = \frac{1}{\sqrt{1-k^2}}\frac{1}{\sqrt{L_1 C_p}} = \frac{1}{\sqrt{L_2 C_s}}$ and $L_x = (1-k^2)L_1$

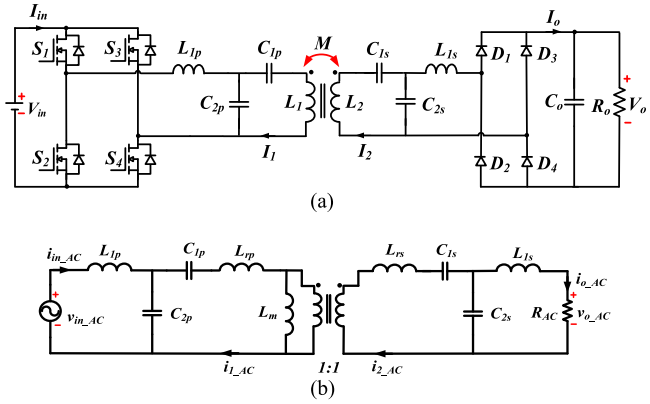

Fig. 2. (a) Double-sided *LCC* compensation topology. (b) AC equivalent circuit of double-sided *LCC* compensation topology.

Table I shows a comparison of the four IPT topologies in terms of their capability to implement the CC/CV charge and to achieve the ZPA condition. It is noticed from this table that the CC and CV charge implementation with the ZPA condition cannot be achieved with a single resonant topology. Hence, it is better to adopt another topology which can achieve the CC/CV mode charge with the ZPA condition for a high efficiency wireless power transfer. The double-sided *LCC* topology is selected in this paper, and the design of compensation tank to achieve CC and CV charge with ZPA condition is presented in the rest of Section II.

B. Analysis of the Double-Sided LCC Topology

Fig. 2(a) shows the double-sided *LCC* compensation topology. The circuit consists of a full-bridge inverter, a *LCC*

compensation tank in both sides, a bridge rectifier, and a load network with an output capacitor. The ***T*** model equivalent circuit in Fig. 2(b) is analyzed in the frequency domain based on the First Harmonic Approximation (FHA) for the sake of simplicity [22]. To get the maximum fundamental output voltage, each switch conducts with almost a 50% duty ratio.

The primary compensation tank is composed of a resonant inductor (L_{1p}) and two resonant capacitors (C_{1p} and C_{2p}). Here, C_{1p} and C_{2p} are connected in series and in parallel with the primary coil, respectively. Similarly, the secondary compensation tank is composed of L_{1s}, C_{1s}, and C_{2s}. To simplify the analysis and design of the IPT system, it is assumed that the number of turns of the primary side coil is equal to that of the secondary side coil. The coil is modeled by a ***T*** model. The relationships among the self-inductances L_1 and L_2, the leakage inductances L_{rp} and L_{rs}, and the coupling coefficient k can be expressed as follows:

$$k = \frac{M}{\sqrt{\left(L_m + L_{rp}\right)\left(L_m + L_{rs}\right)}} = \frac{M}{\sqrt{L_1 L_2}} \tag{3}$$

where M and L_m are the mutual inductance and the magnetizing inductance between the two coils, respectively. The first harmonic components, based on the equivalent circuit in Fig. 2(b), can be written as

$$\begin{aligned} L_{rp} &= (1 - k)\, L_1, \quad L_{rs} = (1 - k)\, L_2 \\ v_{\text{in\_AC}}(t) &= \frac{4}{\pi} V_{\text{in}} \sin(2\pi f t), \; v_{o\_\text{AC}}(t) = \frac{4}{\pi} V_o \sin(2\pi f t + \theta) \\ i_{o\_AC}(t) &= \frac{\pi}{2} I_o \sin(2\pi f t + \theta), \; R_{AC} = \frac{8}{\pi^2}\frac{V_o}{I_o} = \frac{8}{\pi^2} R_o. \end{aligned} \tag{4}$$

V_{in}, V_o, and I_o represents the values for input dc-link voltage, required output voltage for the battery, and required output current for the battery, respectively. The first harmonic components are subscripted by "AC." θ is the phase difference between $v_{\text{in\_AC}}$ and v_{o_AC}. In the following analysis $\mathbf{V_{in}}$, $\mathbf{V_o}$, $\mathbf{I_{in}}$, $\mathbf{I}_1$, $\mathbf{I}_2$, and $\mathbf{I_o}$ are used to depict the complex form of the corresponding variables. It can be easily deduced from (4) that the voltage conversion ratio of the doubled-side *LCC* topology $|\mathbf{V_o}/\mathbf{V_{in}}|$ is identical to V_o/V_{in}. In the following sections, the load-independent characteristics of the double-sided *LCC* compensation topology are analyzed to show how to implement the CC/CV mode charge.

C. Implementation of the CC Mode Charge With the ZPA Condition

As mentioned above, the implementation of the CC mode charge with the double-sided *LCC* compensation topology can be achieved by operating it as a current source. However, the ZPA condition is not obtained by itself in this mode of operation. Hence, the resonant tank needs to be designed so that the phase of the input impedance is equal to zero. In order to derive the conditions for the CC mode operation and the ZPA, the *M* model is adopted to analyze the output characteristics and the resonant tank at each side of the double-sided *LCC* compensation topology since this can facilitate independent analysis at both sides of the circuit (see Fig. 3).

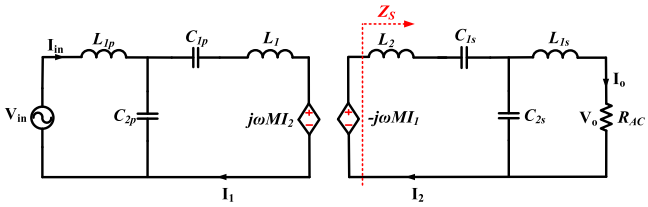

Fig. 3. ***M*** model of double-sided *LCC* compensation topology.

By applying Kirchhoff's law to the ***M*** model in Fig. 3, the voltage equation of the primary side can be obtained as

$$\mathbf{V_{in}} = \left(j\omega L_{1p} - j\frac{1}{\omega C_{2p}}\right)\mathbf{I_{in}} - \frac{1}{j\omega C_{2p}}\mathbf{I}_1. \tag{5}$$

Similarly, the voltage equation of the secondary side can be obtained as

$$j\omega M\mathbf{I}_1 = j\left(\omega L_2 - \frac{1}{\omega C_{2p}} - \frac{1}{\omega C_{2s}}\right)\mathbf{I}_2 + j\frac{1}{\omega C_{2s}}\mathbf{I_o}. \tag{6}$$

It can be easily deduced from (5) and (6) that the input voltage $\mathbf{V_{in}}$ can be expressed only with the output current $\mathbf{I_o}$ and the impedance as (7) if the components of the resonant tank are selected to satisfy the conditions in (8) and (9)

$$\mathbf{I_o} = \frac{\omega_{\text{CC}}^3 C_{2s} C_{2p} M \mathbf{V_{in}}}{j} = \frac{M\mathbf{V_{in}}}{j\omega_{\text{CC}} L_{1p} L_{1s}} \tag{7}$$

$$\omega_{\text{CC}} L_{1p} - \frac{1}{\omega_{\text{CC}} C_{2p}} = 0 \tag{8}$$

$$j\left(\omega_{\text{CC}} L_2 - \frac{1}{\omega_{\text{CC}} C_{1s}} - \frac{1}{\omega_{\text{CC}} C_{2s}}\right) = 0. \tag{9}$$

It can be noticed from (7) that the output current $\mathbf{I_o}$ only depends on the value of the input voltage, the operating frequency, and the parameters of the compensation tank. Hence, it is possible to operate the converter as a current source, thereby implementing the CC mode charge.

On the other hand, an equation for the input impedance needs to be derived to find out the condition for the ZPA. The secondary side impedance Z_S can be derived as (10) with the condition in (9)

$$\begin{aligned} Z_S &= j\left(\omega L_2 - \frac{1}{\omega C_{1s}} - \frac{1}{\omega C_{2s}}\right) // \left(j\omega L_{1s} + R_{\text{AC}}\right) \\ &= \frac{1}{\omega^2 R_{\text{AC}} C_{2s}^2 + j\omega C_{2s}\left(\omega^2 L_{1s} C_{2s} - 1\right)}. \end{aligned} \tag{10}$$

The equivalent impedance of the secondary side referred to the primary side Z_R can be represented by (11). Consequently, the ***M*** model of the double-sided *LCC* compensation topology becomes even simpler, as shown in Fig. 4

$$Z_R = \frac{j\omega M\mathbf{I}_2}{\mathbf{I}_1} = \frac{-(\omega M)^2}{Z_S}. \tag{11}$$

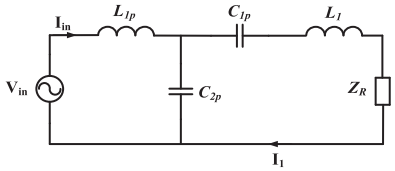

Fig. 4. Simplified ***M*** model of double-sided *LCC* compensation topology.

The input impedance Z_{in} of the simplified M model of the double-sided *LCC* compensation topology in Fig. 4 can be represented as (12), where $Z_N = j(\omega L_1 - 1/\omega C_{1p} - 1/\omega C_{2p})$

$$Z_{\text{in}} = j\left(\omega L_{1p} - \frac{1}{\omega C_{2p}}\right) + \frac{1}{\omega^2 C_{2p}^2\left[Z_N - \frac{(\omega M)^2}{Z_S}\right]}. \quad (12)$$

In order to achieve the ZPA condition at the resonant frequency, the imaginary part of Z_{in} should be zero. In the CC mode operation, the first term in the right-hand side of the (12) is equal to zero at the resonant frequency, as shown in (8). Hence, only the imaginary part of the second term needs to be zero and it can be expanded as shown in (13) at the bottom of this page.

It can be seen from (13) that it becomes a real number if (14) and (15) are satisfied at the angular resonant frequency ω_{CC}

$$\omega_{\text{CC}}^2 L_{1s} C_{2s} - 1 = 0 \quad (14)$$

$$\omega_{\text{CC}} L_1 - \frac{1}{\omega_{\text{CC}} C_{1p}} - \frac{1}{\omega_{\text{CC}} C_{2p}} = 0. \quad (15)$$

Therefore, in order to achieve the ZPA condition during the CC mode charge, the resonant tank needs to be designed to satisfy all of the conditions in (8), (9), (14), and (15) at the angular resonant frequency ω_{CC}, as shown in the following:

$$\omega_{\text{CC}} = \frac{1}{\sqrt{L_{1p}C_{2p}}} = \sqrt{\frac{(C_{1s}+C_{2s})}{C_{1s}C_{2s}L_2}} = \frac{1}{\sqrt{L_{1s}C_{2s}}} = \sqrt{\frac{(C_{1p}+C_{2p})}{C_{1p}C_{2p}L_1}}. \quad (16)$$

D. Implementation of the CV Mode Charge With the ZPA Condition

This section focuses on implementing the CV mode charge operation. In the specifications of the IPT charger in this paper, since the voltage gain of V_o/V_{in} is approximately equal to unity, the self-inductance of the primary coil is the same as that of the secondary coil ($L_1 = L_2$). To simplify the mathematical analysis, it is assumed that the values for the resonant components in the primary side are the same as those in the secondary side

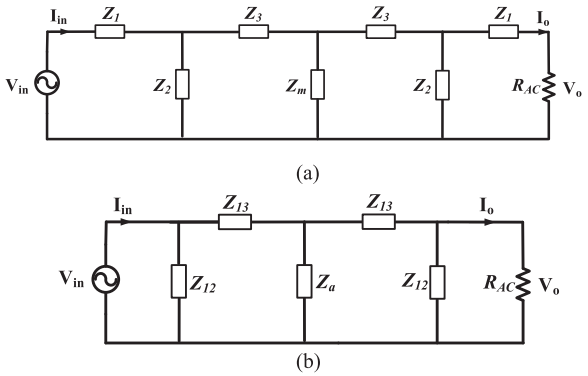

Fig. 5. (a) Simplified equivalent circuit of Fig. 2(b). (b) Further simplified equivalent circuit by applying $\Upsilon - \Delta$ transform.

as follows:

$$\begin{cases} L_{1p} = L_{1s} \\ C_{1p} = C_{1s} \\ C_{2p} = C_{2s} \end{cases}. \quad (17)$$

To facilitate the analysis, the ac equivalent circuit of the double-sided *LCC* compensation topology in Fig. 2(b) is further simplified to the circuit in Fig. 5 by using a Υ–Δ transform. Where

$$\begin{cases} Z_m = j\omega L_m \\ Z_1 = j\omega L_{1p} = j\omega L_{1s} \\ Z_2 = \frac{1}{j\omega C_{2p}} = \frac{1}{j\omega C_{2s}} \\ Z_3 = \frac{1}{j\omega C_{1p}} + j\omega L_{rp} = \frac{1}{j\omega C_{1s}} + j\omega L_{rs}. \end{cases} \quad (18)$$

Therefore, the voltage gain of the double-sided *LCC* compensation topology can be obtained by applying Kirchhoff's voltage law to the model in Fig. 5, as shown in the following:

$$\begin{aligned} G_V &= \left|\frac{\mathbf{V_o}}{\mathbf{V_{in}}}\right| = \frac{V_o}{V_{\text{in}}} \\ &= \left|\frac{Z_a\,(Z_{12}||R_{\text{AC}})}{(Z_{12}||R_{\text{AC}})\,(Z_{13}+Z_a) + Z_{13}\,(Z_{13}+Z_a) + Z_{13}Z_a}\right| \\ &= \left|\frac{Z_a}{Z_{13}+Z_a+\frac{Z_{13}(Z_{13}+2Z_a)}{Z_{12}}} + \frac{Z_{13}\,(Z_{13}+2Z_a)}{R_{\text{AC}}}\right| \end{aligned} \quad (19)$$

Where $Z_{12} = Z_1 + Z_2 + \frac{Z_1 Z_2}{Z_3}$, $Z_{13} = Z_1 + Z_3 + \frac{Z_1 Z_3}{Z_2}$, $Z_{23} = Z_2 + Z_3 + \frac{Z_2 Z_3}{Z_1}$, $Z_a = \frac{Z_m Z_{23}}{2Z_m + Z_{23}}$.

It is easy to see from (19) that the voltage gain G_V becomes constant regardless of the load resistance R_{AC} if (20) is satisfied at the angular resonant frequency ω_{CV}

$$Z_{13}\,(\omega_{\text{CV}})\,[Z_{13}\,(\omega_{\text{CV}}) + 2Z_a\,(\omega_{\text{CV}})] = 0. \quad (20)$$

Hence, the CV mode operation is possible when either (21) or (22) is satisfied. As long as either (21) or (22) is satisfied, the

$$\frac{1}{\omega^2 C_{2p}^2\left[Z_N - \frac{(\omega M)^2}{Z_S}\right]} = \frac{1}{\omega^2 C_{2p}^2\left[j\left(\omega L_1 - \frac{1}{\omega C_{1p}} - \frac{1}{\omega C_{2p}}\right) - j\omega C_{2s}\left(\omega^2 L_{1s} C_{2s} - 1\right)(\omega M)^2 - (\omega M)^2 \omega^2 R_{\text{AC}} C_{2s}^2\right]} \quad (13)$$

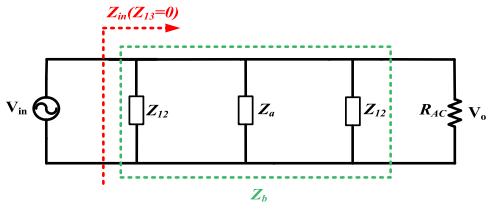

Fig. 6. AC equivalent circuit of the double-sided *LCC* compensation topology when $Z_{13} = 0$.

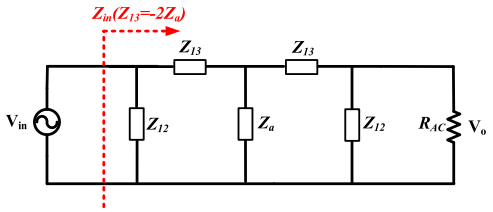

Fig. 7. AC equivalent circuit of double-sided *LCC* compensation topology when $Z_{13} = -2Z_a$.

voltage gain G_V in (19) is unity

$$Z_{13}(\omega_{\mathrm{CV}}) = j\frac{\left[-1+\omega_{CV}^2 C_{1p}\left(L_{1p}+L_{rp}\right)-\omega_{CV}^4 L_{1p}L_{rp}C_{1p}C_{2p}\right]}{\omega_{\mathrm{CV}}C_{1p}} = 0 \tag{21}$$

$$Z_{13}(\omega_{\mathrm{CV}}) + 2Z_a(\omega_{\mathrm{CV}}) = \frac{2Z_m Z_{23} + Z_{13}(Z_{23}+2Z_m)}{Z_{23}+2Z_m} = 0. \tag{22}$$

When $Z_{13} = 0$, Fig. 5 can be redrawn as Fig. 6. In this case the impedance of the resonant tank can be calculated as $Z_b = Z_{12}Z_a/(2Z_a + Z_{12})$ and the input impedance of the circuit can be expressed by

$$Z_{\mathrm{in}}(Z_{13}=0) = \frac{Z_b R_{\mathrm{AC}}}{Z_b + R_{\mathrm{AC}}} = \frac{Z_{12}Z_a R_{\mathrm{AC}}}{R_{\mathrm{AC}}(2Z_a+Z_{12}) + Z_a Z_{12}}. \tag{23}$$

It can be seen from (18) and (19) that Z_{12}, Z_a, and Z_b are all imaginary complex numbers. Therefore, $Z_{\mathrm{in}}(Z_{13}=0)$ can be expressed in complex form as (24) by replacing Z_b with jK

$$Z_{\mathrm{in}}(Z_{13}=0) = \frac{Z_b R_{\mathrm{AC}}}{Z_b + R_{\mathrm{AC}}} = \frac{K^2 R_{\mathrm{AC}}^2}{K^2 + R_{\mathrm{AC}}^2} + j\frac{K R_{\mathrm{AC}}^2}{K^2 + R_{\mathrm{AC}}^2}. \tag{24}$$

In order to achieve the ZPA condition in the CV mode charge, the imaginary part of the input impedance in (24) needs to be zero at the resonant frequency. Therefore, $K = 0$, hence $Z_b = 0$. However, this is impractical since power cannot be transferred to the load when $Z_b = 0$. As a result, the condition in (21) is found to be invalid for achieving the ZPA condition in the CV mode charge.

When the condition in (22) is satisfied, the model in Fig. 5 can be redrawn as Fig. 7. In this case, the input impedance of

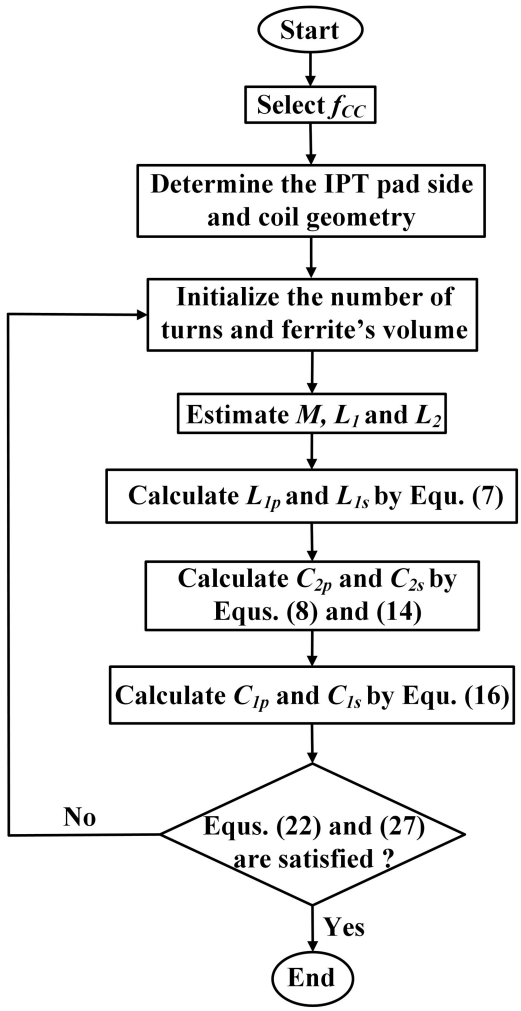

Fig. 8. Design procedure of the proposed IPT Charger.

the converter can be calculated as follows:

$$Z_{\mathrm{in}}(Z_{13} = -2Z_a) = Z_{12}||\{Z_{13} + Z_a||[Z_{13} + (Z_{12}||R_{\mathrm{AC}})]\}. \tag{25}$$

Here, the imaginary part of $Z_{\mathrm{in}}(Z_{13} = -2Z_a)$ can be calculated as

$$\mathbf{Im}[Z_{\mathrm{in}}(Z_{13}=-2Z_a)] = \frac{A_1 R_{\mathrm{AC}}^4 + A_2 R_{\mathrm{AC}}^2}{\left[(A-2B+E)^2+F^2\right]\left[(B+C)^2+D^2\right]\left(A^2+R_{\mathrm{AC}}^2\right)^2} \tag{26}$$

where: $A_1 = Z_a Z_{12}^5(2Z_a - Z_{12})$, $A_2 = Z_a Z_{12}^3(2Z_a - Z_{12})$, and A, B, C, D, E, F are shown in the Appendix.

The derivation procedure for (26) can be found in the Appendix. In order to achieve the ZPA condition in the CV mode charge, the denominator of the right-hand side of (26) needs to be zero. This means that both A_1 and A_2 have to be zero, which can be achieved if (27) is satisfied at the angular resonant frequency ω_{CV}

$$2Z_a(\omega_{\mathrm{CV}}) - Z_{12}(\omega_{\mathrm{CV}}) = 0. \tag{27}$$

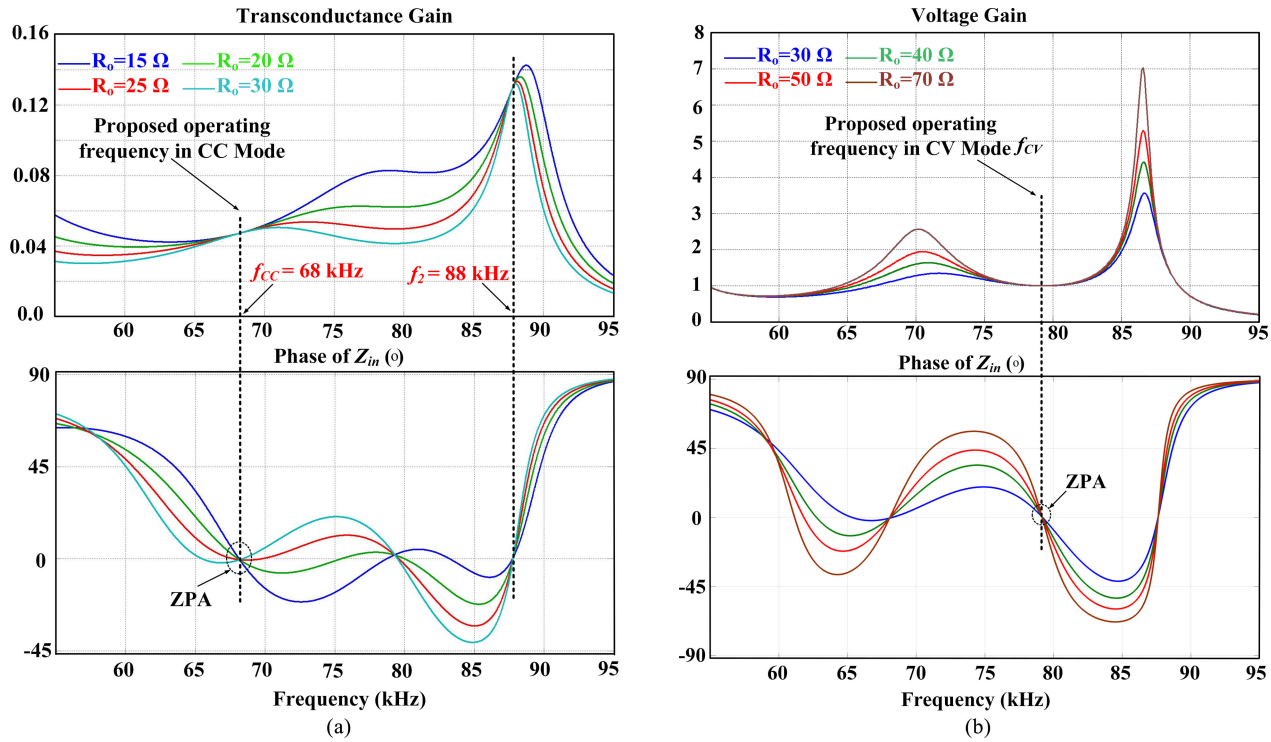

Fig. 9. (a) Transconductance gain and the phase of input impedance of the IPT converter. (b) Voltage gain and phase of input impedance of the IPT converter (when $C_{1p} = C_{1s} = 33\,\text{nF}, C_{2p} = C_{2s} = 102\,\text{nF}, L_m = 57.3\,\mu\text{H}, L_{rp} = L_{rs} = 161\,\mu\text{H}$, and $L_{1p} = L_{2p} = 53.1\,\mu\text{H}$).

If both (22) and (27) are satisfied, the double-sided *LCC* compensation topology can achieve the CV mode charge while achieving the ZPA condition at the angular resonant frequency ω_{CV}. However, the practical design procedure requires some iterations to determine a set of parameters for the resonant tank to satisfy the conditions for the CC and CV mode charge together, as shown in Fig. 8.

The flowchart in Fig. 8 illustrates the practical design procedure for designing the resonant tank for the IPT converter for the CC/CV charge. First of all, the operating frequency in the CC mode charge f_{CC} needs to be selected by considering the volume and loss of the resonant components [1]. Typically, the switching frequency for an IPT system is selected between 20 and 95 kHz [4]–[8]. In this paper, an operating frequency of 68 kHz is selected. In the next step, the size of IPT pads and coil geometry are determined based on the airgap between coils and limitations of the installation area. Next, the number of turns and ferrite's volume are initialized to estimate values for M, L_1, and L_2 by using electromagnetic field simulation software such as MAXWELL. Then, L_{1p} and L_{1s} can be determined from (7) under the assumption that L_{1p} and L_{1s} have the same value. The value for C_{2p} and C_{2s} can be calculated by using (8) and (14), respectively. Similarly, C_{1p} and C_{1s} can be calculated by (16). This set of parameters for the resonant tank can achieve the CC mode charge with the ZPA condition.

At this point it is also necessary to see if the set of parameters calculated to achieve the CC mode charge with the ZPA condition can also satisfy the conditions for the CV mode charge with the ZPA condition by using (22) and (27). Some computer software such as MATLAB software can be a useful tool to check if all of the conditions for implementing the CC/CV mode charge with the ZPA condition are satisfied. If the results are not satisfied, then the values for M, L_1, and L_2 need to be adjusted by varying the number of turns and ferrite's volume, and the procedure explained above needs to be repeated.

TABLE II
SPECIFICATION OF THE IPT BATTERY CHARGER

P_o	Power rating	6.6 [kW]
V_{in}	Input voltage	400 [DC]
V_o	Output voltage	250–420 [V]
I_o	Charge current	15.7[A]

E. Verification of the Proposed Design for the CC/CV Mode Charge

In order to verify the proposed design method, the graphs for the transconductance gain G_I and the phase of the input impedance Z_{in} are drawn as shown in Fig. 9(a), and those for the voltage gain G_V and the phase of the input impedance Z_{in} are drawn as shown in Fig. 9(b). The specification of the IPT charger can be found in Table II and all the parameters of resonant tank can be calculated by the aforementioned design rules.

As clearly illustrated in Fig. 9(a), the transconductance gain G_I is constant regardless of the load, and the ZPA condition is achieved at the operating frequency f_{CC} (68 kHz). There are two frequencies (68 and 88 kHz) to realize CC output and ZPA. However, 68 kHz is selected for CC output and ZPA due to the following reasons. The slope of the transconductance gain

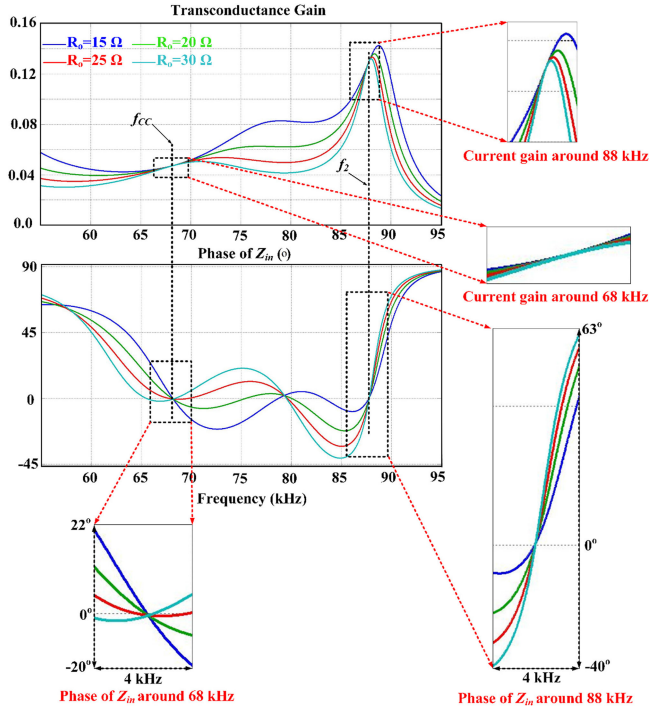

Fig. 10. Variations of the transconductance gain and the phase of input impedance around 68 and 88 kHz in CC mode operation.

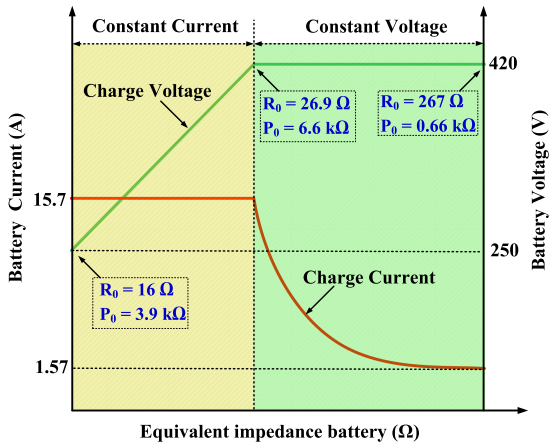

Fig. 11. CC/CV Charge profile of the battery and equivalent impedance of the EV battery.

TABLE III
IPT COILS SYSTEM PARAMETERS

L_1	Self-inductance of transmitter coil	218.3 μH
L_2	Self-inductance of receiver coil	218.3 μH
M	Magnetizing inductance	57.3 μH
k	Coupling factor	0.262
Q	Quality factor	4.3
d	Distance	200 mm
n	Number of turns (Litz wire-600 strands-AWG 38)	7
	Size of DD type pad	460 cm^2 (66 cm × 66 cm)
	Ferrite bars	6
	Ferrite pieces (14.5 cm × 3.5 cm × 1.6 cm)	24

curve at 88 kHz is significantly higher than that at 68 kHz, as shown in Fig. 10. Therefore, the variation of the output current I_o at 88 kHz is more sensitive to the variation of the switching frequency than that at 68 kHz. A small change in frequency around 88 kHz can lead to a significant variation of the output current. In addition, the phase of Z_{in} at 88 kHz is significantly stiffer than that at 68 kHz. Therefore, the variation of the phase according to the switching frequency variation at 88 kHz is larger than that at 68 kHz. While the variation of the phase of Z_{in} within ±2 kHz at 88 kHz is 103° (–40° to 63°), it is 42° (–20° to 22°) within ±2 kHz at 68 kHz. Therefore, 68 kHz is preferred in terms of the stability of the control since it shows smaller variations in transconductance gain and phase of Z_{in}.

As shown in Fig. 9(b), the voltage gain is constant regardless of the load, and ZPA condition is achieved at the operating frequency f_{CV} (79.1 kHz). It can be verified from Fig. 9 that the proposed design method allows the IPT converter to operate in the CC and CV mode with the ZPA condition.

III. DESIGN CONSIDERATIONS

In this section, some design considerations for the design of the IPT coils and double-sided *LCC* tank for a 6.6-kW IPT charger to achieve the CC/CV charge for EV batteries (see Fig. 11) is presented.

A. Design of the IPT Pads

In an IPT battery charger system, the IPT pads play an integral role. The efficiency of the system mainly depends on the coupling coefficient k and quality factor Q of the coil. Generally, the coupling coefficient k depends on the ratio between the dimensions of the pads and the air gap, the number of turns, and the number of ferrite bars for a given structure. Hence, the IPT pads need to be designed to have higher values for k and Q with minimum volume and weight since their values are quite different depending on the structure of the pads. Through a comparison of the coil structures in terms of k and Q, DD type pads have been selected [23]. This is also advantageous in that a better tolerance for horizontal misalignment can be obtained with DD type pads since they have the highest fundamental flux path height. In this paper, the DD type pads are designed and implemented, as shown in Table III and Fig. 12 based on the design procedure in Fig. 8.

B. Design of the LCC Compensation Tank

The values for the ac inductors L_{1p} and L_{1s} can be calculated as (28) by using (7) to achieve the CC mode with a 15.7 A charge current

$$L_{1p} = L_{1s} = \sqrt{\frac{8\text{MV}_{\text{in}}}{(2\pi f_{\text{CC}})\,\pi^2 I_o}} \approx 57.3\ \mu\text{H}. \tag{28}$$

It should be noted that an air core needs to be used for the ac inductor instead of a magnetic core since the voltage across the ac inductor is quite high due to resonance. If the magnetic core is adopted in this situation, then it requires a very large core to cope with saturation problem when the inductor operates under

Fig. 12. Employed DD structure coil for 6.6 kW IPT charger.

TABLE IV
RESONANT TANK PARAMETERS

L_{1p}	Primary Additional Inductor	53.1 μH
L_{2s}	Self-inductance of receiver coil	53.1 μH
C_{2p}	Primary Parallel Capacitor	102 nF
C_{2s}	Secondary Parallel Capacitor	102 nF
C_{1p}	Primary Series Capacitor	33 nF
C_{1s}	Secondary Series Capacitor	33 nF
f_{CC}	Frequency in CC Mode	68 kHz
f_{CV}	Frequency in CV Mode	79.1 kHz

high voltage condition [24]. Here, two ac inductors with an air core and a diameter of 7 cm are used. All of the measured values of the resonant tank components including the capacitors selected by using (8), (14), and (16) can be found in Table IV.

C. Design of the Closed-Loop Controller for the CC/CV Charge

Once the double-sided *LCC* compensation tank is suitably designed according to the design procedure presented in chapter II, the CC and CV mode charge can be simply implemented at each fixed resonant frequency while achieving the ZPA condition in both modes. However, a small variation in the operating frequency at different output powers is attributed to a small error in the IPT charger model caused by the FHA and the neglect of the resistances in the resonant components. Furthermore, the switching frequency for primary inverter needs to change automatically depending upon CC and CV mode charge in practical situation. Therefore, closed-loop control is necessary to achieve the CC and CV mode charge operation while maintaining the ZPA condition. The closed-loop control structure with a simple PI control is adopted, as shown in Fig. 13(a). The controller is composed of a mode charge selection, a current controller, a voltage controller, and a voltage controlled oscillator. Since each mode charge of the control requires its own independent controller, one of two is selected by the mode selection according to the mode of charge. The mode selection selects mode charges depending on the battery voltage. When

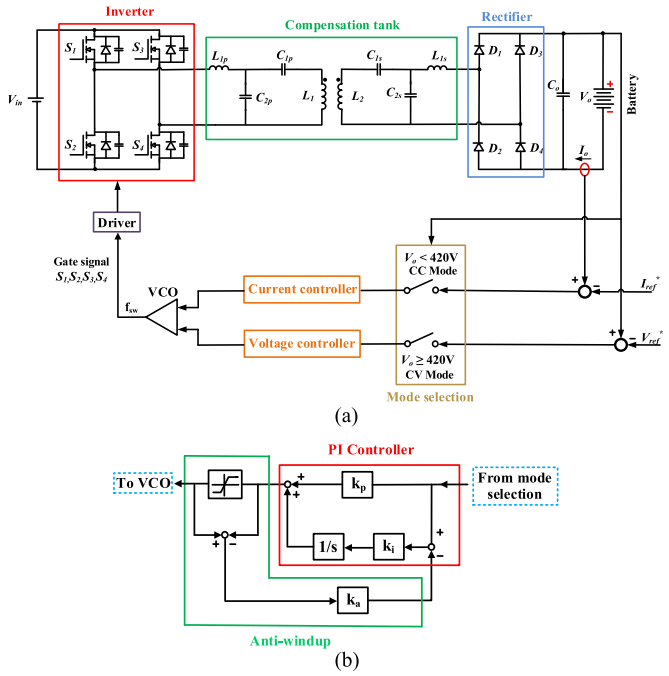

Fig. 13. (a) Closed-loop control strategy of the proposed IPT charger system. (b) Structure of the current or voltage controller.

the battery voltage is lower than the maximum charge voltage, 420 V in this paper, the current controller is activated to charge the battery with the CC mode while the voltage controller is deactivated. Once the voltage of the battery reaches its maximum charge voltage, the current controller is automatically switched OFF and the voltage controller is switched ON to charge the battery in CV mode charge. The current or voltage controller is composed of a PI controller, a frequency limiter, an antiwindup scheme and its structure is demonstrated in Fig. 13(b). The limiters are used in both current and voltage controller to prevent the IPT charger from operating at undesirable frequencies. In CV mode, the operating frequency is adjusted slightly lower than f_{CV} to achieve higher voltage gain and ensure that the IPT converter can always operate in the inductive region. The antiwindup scheme is added to reduce the transient time and overshoot caused by the limiter operation.

In order to design the PI controllers, transfer functions for each mode of operation need to be derived. However, in case of resonant converter, it is very complex to derive the transfer function by using traditional method such as the small-signal analysis due to high order of the state-space model. Instead of deriving the transfer function, the ac sweeping function in Power Sim software [26] is used to draw the bode plots for the control-to-output current and control-to-output voltage transfer functions, which is also mentioned in [27]. Fig. 14(a) and (b) show bode plots for the current control and voltage control under different load conditions, respectively. The PI controller is designed to provide enough of a phase margin at the crossover frequency for each mode of charge. The phase margin and bandwidth of the current controller are 600 Hz and 70°, respectively, then the

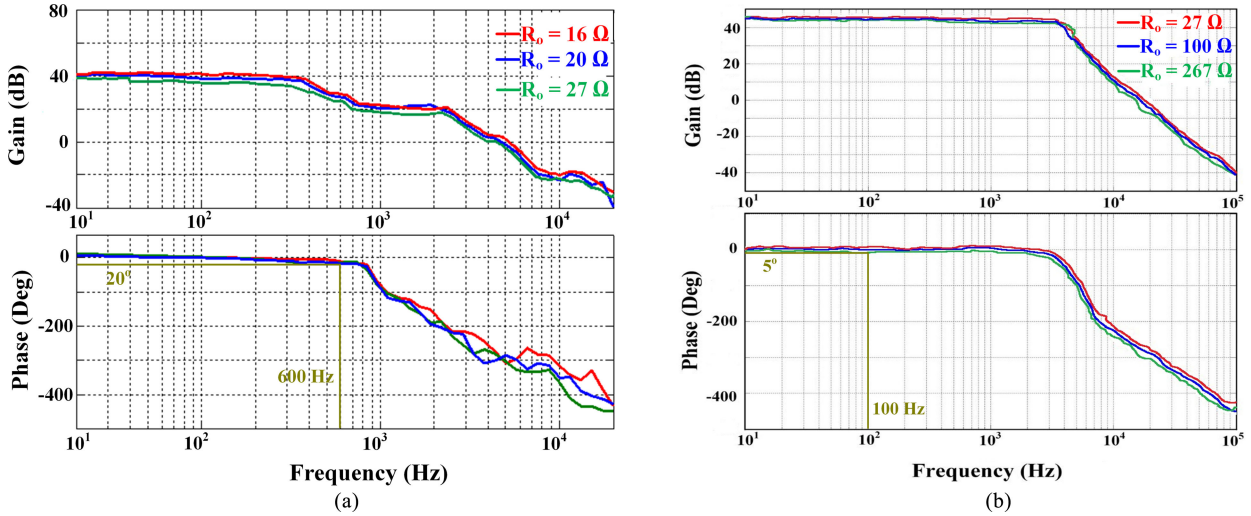

Fig. 14. Bode plots for open-loop converter under different load conditions. (a) CC mode operation at 68 kHz. (b) CV mode operation at 77.5 kHz.

PI current controller is designed as shown in the following:

$$G_{ci}(s) = 0.005 + \frac{10}{s}. \tag{29}$$

Similarly, the PI voltage controller is designed to achieve the phase margin and bandwidth of 85° and 100 Hz, respectively, as shown in (30):

$$G_{cv}(s) = 0.003 + \frac{16.67}{s}. \tag{30}$$

IV. Experimental Results and Discussion

A prototype of 6.6-kW IPT charger is implemented and tested to demonstrate its validity and feasibility. A picture of the experimental setup is shown in Fig. 15. Here, four MOSFETs (IXFB120N50P2, 43 mΩ R_{ds_ON}) are used for the full-bridge inverter, and four fast-recovery diodes (HFA50PA60) are used for the rectifier. Polypropylene film capacitors are used for the resonant capacitors due to their lower equivalent series resistance and higher current carrying capability. In order to meet the voltage and current ratings of the double-sided *LCC* compensation tank, each resonant capacitor is implemented by using four discrete capacitors. A picture of primary coil and compensation tanks including resonant inductors and capacitors are shown in Fig. 15(a) and (b). All of the closed-loop controllers are implemented with a Texas Instruments TMS320F28335 DSP. The battery current and voltage are sensed by a LEM LA 55-P current transducer and LEM LV 25-P voltage transducer, respectively. In practical applications a wireless feedback circuit should be designed and implemented for the voltage and current regulation of the IPT charger and it can be implemented with no difficulty by using a Bluetooth module such as the LMX9838 from Texas Instrument. In this paper, however, we have focused on introducing a novel technique to implement the CC and CV charge of an IPT system with the double-sided *LCC* compensation topology for EV battery charge applications. Hence, the wired connections for the feedback signals have been used for simplicity.

The efficiency of the IPT converter is measured by a YOKOGAWA WT1600 Power Analyzer and the waveforms are captured by a Lecroy Wave Runner 604Zi oscilloscope. A Chroma dc Electronic Load 63204 is used to emulate the EV battery.

Prior to a discussion about the experimental results it should be pointed out that there are two options for operating the proposed IPT charger in the CV mode. It is noted that the input voltage V_{in} of the proposed IPT charger from the front-end ac/dc converter varies between 380 to 420 V (400 V ± 5%). One option is to regulate the output voltage of the front-end ac/dc converter to be 420 V in order to have 420 V at the output of the IPT converter since the converter is designed to have a unity voltage gain. The other option is to adjust the operating frequency slightly to get a higher voltage gain 1.05, to obtain 420 V with a 400 V input. Here, it is possible to get the right gain by increasing or decreasing the operating frequency little bit. Since the ZVS operation is preferred for MOSFET inverters, it is desirable to lower the switching frequency little bit for operation in the inductive region.

Fig. 16 shows experimental waveforms of the implemented IPT converter during the CC mode charge with a 400 V input. As shown in Fig. 16(a), the output current I_o is constant at 15.7 A, 3.9 kW and the switching frequency is 67.5 kHz. Fig. 16(b) shows waveforms of the IPT converter at 6.6 kW during the CC mode charge and the switching frequency is 68.3 kHz. It is clearly shown in both figures that the ZVS and ZCS of the switches are perfectly achieved since the ZPA condition is achieved during the CC mode charge. When the power is increased, the operating frequency from controller varied a little bit from 67.5 to 68.3 kHz to keep the output current constant.

Fig. 17 shows experimental waveforms of the implemented IPT converter during the CV mode charge with a 400 V input. As shown in Fig. 17(a), the output voltage V_o is kept constant at 420 V, 5.88 kW, and the operating frequency is 76.8 kHz. Fig. 17(b) shows waveforms of the IPT converter at 2.52 kW during the CV mode charge, and the operating frequency is 77.5 kHz. It is shown in both figures that only the ZVS is achieved since the IPT converter operates in the inductive region.

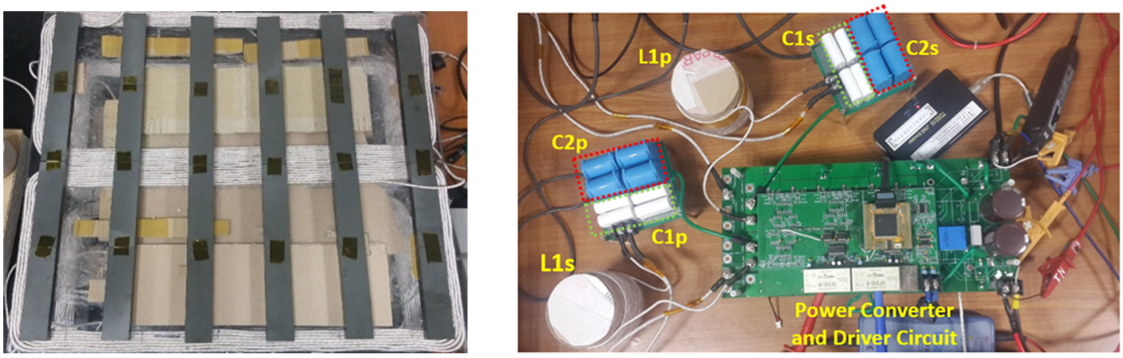

(a) (b)

Fig. 15. Experimental Setup for double-sided *LCC* IPT charger. (a) Primary coil. (b) Compensation tanks and power converter circuit.

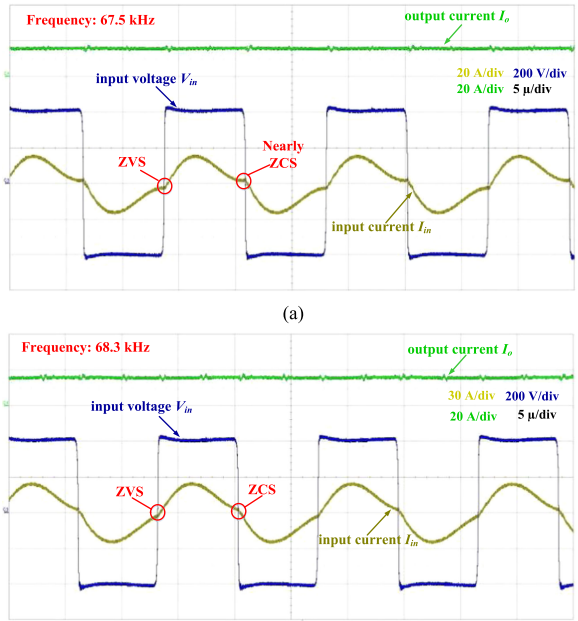

Fig. 16. Experimental waveforms of V_{in}, I_{in}, and I_o in CC mode operation with 400 V input. (a) $P_o = 3.9\,\text{kW}$. (b) $P_o = 6.6\,\text{kW}$.

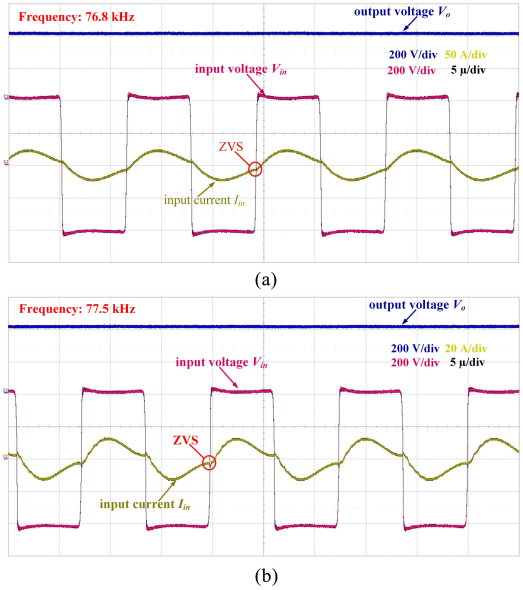

Fig. 17. Experimental waveforms of V_{in}, I_{in}, and V_o in CV mode operation with 400 V input. (a) $P_o = 5.88\,\text{kW}$. (b) $P_o = 2.52\,\text{kW}$.

In the CV mode, the operating frequency from the controller varied a little bit from 76.5 to 77.8 kHz to keep the output voltage constant. As mentioned earlier, the IPT converter operates at a slightly lower frequency than the resonant frequency (79.1 kHz) to get a higher voltage gain.

Fig. 18 shows experimental waveforms when the input voltage of the IPT converter is 420 V during the CV mode charge. The IPT charger can operate at around f_{CV} value due to unity voltage gain. The ZVS and ZCS of the switch are perfectly achieved since the ZPA condition is achieved during the CV mode charge. Here, the operating frequencies under both conditions are also slightly different due to the reasons previously mentioned.

A significant benefit of the proposed method is that the operating frequency is almost constant during the CC or CV mode charge regardless of the load. In consequence, the design of the controller is simpler and it is easier to guarantee the reliability of the IPT charger.

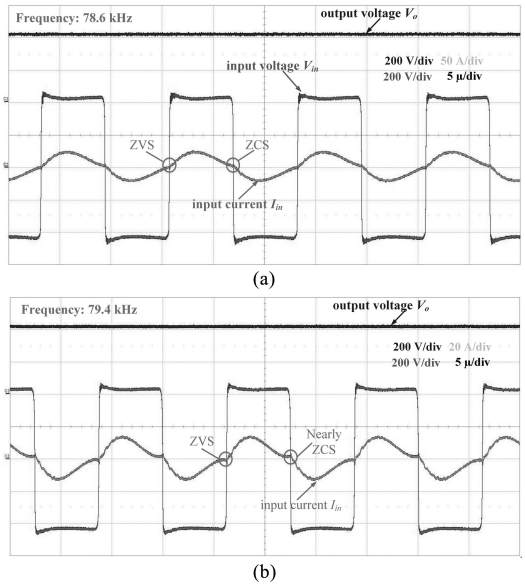

Fig. 18. Experimental waveforms of V_{in}, I_{in}, and V_o in CV mode operation with 420 V input. (a) $P_o = 5.88\,\text{kW}$. (b) $P_o = 2.52\,\text{kW}$.

$$\mathrm{Im}\left[Z_{\mathrm{in}}\left(Z_{13}=-2Z_a\right)\right]=\frac{A\left[-D^2BA+B^2\left(C^2+D^2\right)+4B^3\left(B\ +\ C\right)-AB\left(B\ +\ C\right)\left(C\ +\ 2B\right)\right]}{\left[\left(A-2B+E\right)^2+F^2\right]\left[\left(B\ +\ C\right)^2+D^2\right]} \tag{A4}$$

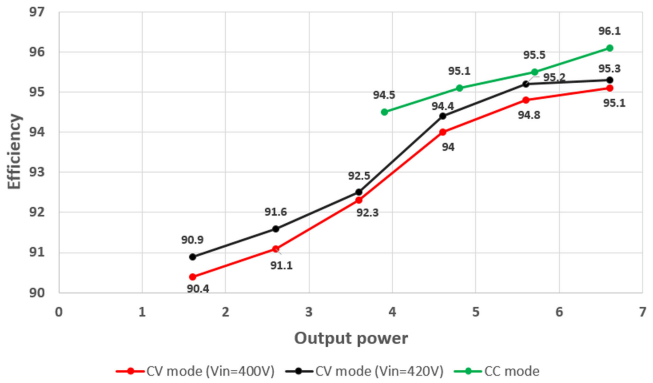

Fig. 19. Efficiency of the proposed IPT converter over CC/CV charge profile.

Fig. 19 shows the efficiency of the IPT converter at different output powers over the CC/CV charge profile. The peak efficiency is 96.1% at 6.6 kW under the CC mode charge. In the CV mode charge operation, the efficiency of the IPT converter with a 420 V input is slightly higher than that with a 400 V input, thanks to the perfect resonant operation with the ZPA condition.

V. Conclusion

In this paper, a novel method to achieve the CC/CV charge of IPT systems with a double-sided *LCC* compensation tank for EV battery charge applications was presented. The frequency characteristics of the double-sided *LCC* compensation tank are precisely analyzed to achieve both of load-independent current and voltage characteristics with the ZPA condition at two different resonant frequencies. A design procedure and a control method were proposed to implement the CC and CV charge. The proposed IPT charger can overcome most drawbacks of conventional IPT charger in terms of cost, complexity, efficiency, and power capability during the entire charge operation. One additional benefit of the proposed method is that the CC/CV charge can be implemented at an almost fixed frequency, which makes it easier to design the controller and to guarantee the reliability of the system. The superior performance of the proposed system in terms of its high efficiency and reliable operation has been verified through experimental results.

Appendix

Derivation procedure for the imaginary part of input impedance Z_{in} in (26) under the conditon of $Z_{13}+2Z_{\mathrm{a}}=0$.

In Fig. 20, $Z_{\mathrm{in}}\left(Z_{13}=-2Z_a\right)$ can be derived as follows:

$$Z_{\mathrm{in}}\left(Z_{13}=-2Z_a\right)=\frac{jAF-A\left(E\ -\ 2B\right)}{j\left(A-2B+E\right)+F} \tag{A1}$$

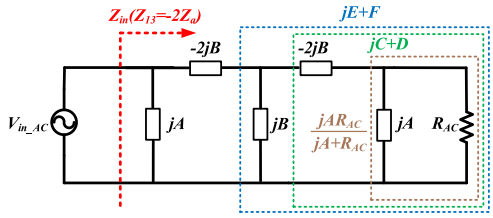

Fig. 20. AC Equivalent circuit of double-sided *LCC* compensation topology when $Z_{13}=-2Z_a$ by adopting A, B, C, D, E, and F.

where A, B, E, F are determined as follows:

$$\begin{cases} A=Z_{12}/j;\ B=Z_a/j \\ C=-2B+\left(AR_{\mathrm{AC}}^2\right)/\left(A^2+R_{\mathrm{AC}}^2\right) \\ D=\left(AR_{\mathrm{AC}}^2\right)/\left(A^2+R_{\mathrm{AC}}^2\right) \\ E=\left[D^2B+\left(B\ +\ C\right)BC\right]/\left[D^2+\left(B\ +\ C\right)^2\right] \\ F=\left[-BCD+\left(B\ +\ C\right)BC\right]/\left[D^2+\left(B\ +\ C\right)^2\right] \end{cases}. \tag{A2}$$

The imaginary part of $Z_{\mathrm{in}}\left(Z_{13}=-2Z_a\right)$ can be calculated as

$$\mathrm{Im}\left[Z_{\mathrm{in}}\left(Z_{13}=-2Z_a\right)\right]=\frac{AF^2-A\left(E\ -\ 2B\right)\left(A-2B+E\right)}{\left(A-2B+E\right)^2+F^2}. \tag{A3}$$

By substituting E and F in (A2) into the numerator of (A3), $\mathrm{Im}[Z_{\mathrm{in}}\left(Z_{13}=-2Z_a\right)]$ can be expressed in (A4) as shown as the top of this page.

In order to determine the numerator of (A4), C and D in (A2) are substituted into the numerator of (A4) and the imaginary part of Z_{in} can be represented as

$$\mathrm{Im}\left[Z_{\mathrm{in}}\left(Z_{13}=-2Z_a\right)\right]=\frac{BA^3\left(2B\ -\ A\right)R_{\mathrm{AC}}^4+BA^5\left(2B\ -\ A\right)R_{\mathrm{AC}}^2}{\left[\left(A-2B+E\right)^2+F^2\right]\left[\left(B\ +\ C\right)^2+D^2\right]\left(A^2+R_{\mathrm{AC}}^2\right)^2}. \tag{A5}$$

As a result, A_1 and A_2 can be written as $BA^3(2B-A)$ and $BA^5(2B-A)$, respectively.

References

[1] S. Li and C. C. Mi, "Wireless power transfer for electric vehicle applications," *IEEE J. Emerg. Sel. Topics Power Electron.*, vol. 3, no. 1, pp. 4–17, Mar. 2015.

[2] J. M. Miller, P. T. Jones, J.-M. Li, and O. C. Onar, "ORNL experience and challenges facing dynamic wireless power charging of EV's," *IEEE Power Electron. Mag.*, vol. 15, no. 2, pp. 40–53, May 2015.

[3] C. W. Wang, O. H. Stielau, and G. A. Covic, "Design considerations for a contactless electric vehicle battery," *IEEE Trans. Power Electron.*, vol. 52, no. 5, pp. 1308–1314, Oct. 2005.

[4] U. K. Madawala and D. J. Thrimawithana, "A bidirectional inductive power interface for electric vehicles in V2G systems," *IEEE Trans. Ind. Electron.*, vol. 58, no. 10, pp. 4789–4796, Oct. 2011.

[5] H. H. Wu, A. Gilchrist, K. D. Sealy, and D. Bronson, "A high efficiency 5 kW inductive charger for EVs using dual side control," *IEEE Trans. Ind. Informat.*, vol. 8, no. 3, pp. 585–595, Aug. 2012.

[6] N. A. Keeling, G. A. Covic, and J. T. Boys, "A unity-power-factor IPT pickup for high-power applications," *IEEE Trans. Ind. Electron.*, vol. 57, no. 2, pp. 744–751, Feb. 2010.

[7] Z. Pantic, B. Sanzhong, and S. Lukic, "ZCS LCC-compensated resonant inverter for inductive-power-transfer application," *IEEE Trans. Ind. Electron.*, vol. 58, no. 8, pp. 3500–3510, Aug. 2011.
[8] S. Li, W. Li, J. Deng, T. D. Nguyen, and C. C. Mi, "A double-sided LCC compensation network and its tuning method for wireless power transfer," *IEEE Trans. Veh. Technol.*, vol. 64, no. 6, pp. 2261–2273, Jun. 2015.
[9] W. Li, H. Zhao, S. Li, J. Deng, T. Kan, and C. C. Mi, "Integrated LCC compensation topology for wireless charger in electric and plug-in electric vehicles," *IEEE Trans. Ind. Electron.*, vol. 62, no. 7, pp. 4215–4225, Jul. 2015.
[10] J. Deng, W. Li, T. D. Nguyen, S. Li, and C. C. Mi, "Compact and efficient bipolar coupler for wireless power chargers: Design and analysis," *IEEE Trans. Power Electron*, vol. 30, no. 11, pp. 4215–4225, Nov. 2015.
[11] T. Kan, T. D. Nguyen, J. C. Wjite, R. K. Malhan, and C. C. Mi, "A new integration method for an electric vehicle wireless charging system using LCC compensation topology," *IEEE Trans. Power Electron.*, vol. 32, no. 2, pp. 1638–1650, Feb. 2017.
[12] D. Andrea, *Battery Management Systems for Large Lithium-Ion Battery Packs*, 1st ed. Boston, MA, USA: Artech House, 2010.
[13] C. Zheng *et al.*, "High efficiency contactless power transfer system for electric vehicle battery charging application," *IEEE J. Emerg. Sel. Topics Power Electron.*, vol. 3, no. 1, pp. 65–74, Mar. 2015.
[14] J. Shin *et al.*, "Design and implementation of shaped magnetic-resonance-based wireless power transfer system for roadway-powered moving electric vehicles," *IEEE Trans. Ind. Electron.*, vol. 61, no. 3, pp. 1179–1192, Mar. 2014.
[15] C. W. Wang, G. A. Covic, and O. H. Stielau, "Power transfer capability and bifurcation phenomena of loosely coupled inductive power transfer systems," *IEEE Trans. Ind. Electron.*, vol. 51, no. 1, pp. 148–157, Feb. 2004.
[16] O. Knecht, R. Bosshard, and J. W. Kolar, "High efficiency transcutaneous energy transfer for implantable mechanical heart support systems," *IEEE Trans. Power Electron.*, vol. 30, no. 11, pp. 6221–6236, Nov. 2015.
[17] R. Bosshard, J. W. Kolar, F. Canales, B. Guggisberg, G. Gong, and B. Wunsch, "Inductive power transfer system and method for operating an inductive power transfer system," Patent EP2928038, Oct. 7, 2015.
[18] W. Zhang, S. C. Wong, C. K. Tse, and Q. Chen, "Design for efficiency optimization and voltage controllability of series–series compensated inductive power transfer systems," *IEEE Trans. Power Electron.*, vol. 29, no. 1, pp. 191–200, Jan. 2014.
[19] W. Zhang, S. C. Wong, and C. K. Tse, "Analysis and comparison of secondary series- and parallel-compensated inductive power transfer systems operating for optimal efficiency and load-independent voltage-transfer ratio," *IEEE Trans. Power Electron.*, vol. 29, no. 6, pp. 2979–2990, Jun. 2014.
[20] C. Auvigne, P. Germano, D. Ladas, and Y. Perriard, "A dual-topology ICPT applied to an electric vehicle battery charger," in *Proc. Int. Conf. Electr. Mach.*, 2012, pp. 2287–2292.
[21] X. Qu, H. Han, S. C. Wong, C. K. Tse, and W. Chen, "Hybrid IPT topologies with constant-current or constant-voltage output for battery charging applications," *IEEE Trans. Power Electron.*, vol. 1, no. 1, pp. 6329–6337, Jan. 2015.
[22] R. W. Erickson and D. Maksimovic, *Fundamentals of Power Electronics*, 2nd ed. New York, NY, USA: Academic, 2001.
[23] M. Budhia, J. Boy, G. Covic, and C.-Y. Huang, "Development of a single-side flux magnetic coupler for electric vehicle IPT charging systems," *IEEE Trans. Ind. Electron.*, vol. 60, no. 1, pp. 318–328, Jan. 2013.
[24] M. K. Kazimierczuk and H. Sekiya, "Design of AC resonant inductors using area product method," in *Proc. IEEE Energy Convers. Congr. Expo.*, 2009, pp. 994–1001.
[25] R. Bosshard, J. W. Kolar, and B. Wunsch, "Control method for inductive power transfer with high partial-load efficiency and resonance tracking," in *Proc. IEEE Power Electron. Conf.*, May 2014, pp. 2167–2174.
[26] [Online]. Available: https://powersimtech.com
[27] V. B. Vu, V. T. Doan, V. L. Pham, and W. J. Choi, "A new method to implement the constant current- constant voltage charge of the inductive power transfer system for electric vehicle applications," in *Proc. IEEE Transp. Electrification Conf. Expo., Asia-Pac.*, Busan, South Korea, 2016, pp. 449–453.

Van-Binh Vu (S'17) hails from Vietnam. He received the Bachelor's degree (talented program) from Hanoi University of Science and Technology, Hanoi, Vietnam, in 2014, and the Master's degree from Soongsil University, Seoul, South Korea, in 2016, both in electrical engineering. He is currently working toward the Ph.D. degree in power electronics at the Electrical Power Group, School of Engineering, Newcastle University, Newcastle Upon Tyne, U.K. Since September 2016 his studies have been funded by the Singapore-Newcastle scholarship.

His current research interests include wireless power transfer and resonant converter for electric vehicles.

Mr. Vu has been awarded a travel grant from IEEE Industrial Electronics Society to attend the 26th IEEE International Symposium on Industrial Electronics.

Duc-Hung Tran was born in Bac Giang, Vietnam, in 1991. He received the B.S. degree in electrical engineering from the Hanoi University of Science and Technology, Hanoi, Vietnam, in 2014 and the M.S. degree in electrical engineering from Soongsil University, Seoul, South Korea, in 2017.

His research interests include wireless power transfer, dc–dc converters dealing with the renewable sources and batteries for energy storage systems or hybrid electric vehicles, and soft-switching techniques for pulse width modulation/pulse-frequency modulation converters.

Woojin Choi (S'00–M'05) was born in Seoul, South Korea, in 1967. He received the B.S. and M.S. degrees in electrical engineering from Soongsil University, Seoul, South Korea, in 1990 and 1995, respectively, and the Ph.D. degree in electrical engineering from Texas A&M University, College Station, TX, USA, in 2004.

He was a Research Engineer with Daewoo Heavy Industries, Seoul, South Korea, from 1995 to 1998. In 2005, he joined the School of Electrical Engineering, Soongsil University. His research interests include modeling and control of electrochemical energy sources (such as fuel cells, batteries, and supercapacitors), power conditioning technologies in renewable energy systems, and dc–dc converters for electric vehicles and fuel cells.

Dr. Choi is an Associate Editor of the IEEE TRANSACTIONS ON INDUSTRY APPLICATIONS and a Publication Editor of the *Journal of Power Electronics* of the Korean Institute of Power Electronics.